Water Resour Manage
DOI 10.1007/s11269-014-0676-1

Monitoring Turbid Plume Behavior from Landsat Imagery

R. L. Fernandez · M. Bonansea · M. Marques

Received: 16 December 2012 / Accepted: 13 May 2014

Abstract A simple model based on available Landsat imagery data was used in order to characterize the dynamics of a rainstorm-induced turbid plume into a semi-arid, medium-sized reservoir. Additionally, a set of empirical expressions based on mouth river conditions was employed to estimate the spatial extent of the turbid plume, as well as the influence of the wind on the spreading and resuspension of sediment. This predicted plume behavior was then confirmed by the imagery data. Overall, the main contribution of the paper is a unified procedure of different approaches that can be applied to forecast turbidity effects during muddy inflow events in aquatic systems where minor field-measured information is available. The approach may be also considered as an assisting tool to provide managers with the capacity to develop real-time strategies to monitor flood events.

Keywords Turbid plume · Landsat imagery · Suspended sediment · River inflow · Reservoir

1 Introduction

Wildland fires represent a potentially important threat to the water quality storage reservoirs situated in fire-prone forest catchments. Burn leads to changes in vegetative structure and potentially soil properties which increase the risk of runoff, severe erosion, nutrient enriched sediment production, and the time required for ecosystem recovery (Miller and Yool 2002).

The highly suspended sediment concentrations (*SSC*) that arrive to aquatic resources in response to post-fire flood events, and the reduction of light penetration in aquatic systems associated to these events (e.g. Smith et al. 1999; Shukla et al. 2008) make managers to be

R. L. Fernandez (✉)
National Scientific and Technical Research Council (CONICET), Universidad Nacional de Córdoba, Córdoba, Argentina
e-mail: rocioluz@yahoo.com

M. Bonansea
National Scientific and Technical Research Council (CONICET), National University of Rio Cuarto, Rio Cuarto, Argentina

M. Marques
Estate University of Maringa, Maringa, Brazil

Published online: 14 June 2014

interested in the assessment of suspended sediment loads and plume exposure times in the short term, rather than in the estimates of the average annual sediment loads.

During a rainstorm event, one of the best approaches to understand the extend and temporal variations of *SSC* to support ecology management practices is via remote sensing data. By contrasting with conventional field methods developed to measure *SSC* on aquatic environments (Pavelsky and Smith 2009, as an example), remote sensing techniques are less expensive, low time-consuming and easy to be performed (Ostlund et al. 2001; Wu et al. 2009; Alcantara et al. 2010). Remote sensing of *SSC* is based upon how sediments variations alter the optical properties of the water column (Pavelsky and Smith 2009). The nature of these variations, or the different reflectivities, is mostly due to the diameter of the particles, depth and surface roughness of the suspended sediment. In this context, the simplest models for mapping *SSC* utilize reflectance from a single band in the red portion of the spectrum (Hellweger et al. 2006). However, different studies suggest a combination of red reflectance with other visible bands in order to increase robustness when sediment color varies (Choubey 1994; Han et al. 2006).

Among several satellite systems that have been used with spatial, temporal and radiometric resolution for the study of surface water with relative accuracy, the Landsat system is particularly useful for inlands water (Giardino et al. 2001; Kloiber et al. 2002; Cohen and Goward 2004). The resolutions of Landsat sensor systems make these data highly suitable to analyze or evaluate the concentration of waterborne constituents (e.g., phytoplankton, temperature and suspended sediment), bathymetry, bottom vegetation cover, and in mapping wetland resources at different spatial scales (Hu et al. 2001; Giardino et al. 2001; Peckham 2008; Alcantara et al. 2010).

Most of the methods to estimate *SSC* based on remote sensing they construct empirical relationships between in-situ measurements and remotely sensed reflectance values (Choubey 1994; Schmugge et al. 2002; Pavelsky and Smith 2009; Giardino 2010; Sriwongsitanon et al. 2011). When field data is scarce or it is not available, like in the present study, a theoretical model may be the best way to study both temporal and spatial suspended sediments patterns based on Landsat images.

In assessing turbid plume behavior, the extent of the advectively dominated riverine zone can be taken as the point where the buoyancy equals the advective forces, and so, a number of relationships became available in the existing literature to predict the plunging behavior of the muddy water into a reservoir (e.g. Imberger and Patterson 1990; Parker and Toniolo 2007). For those empirical expressions the hydraulics properties at the river mouth are the initial boundary conditions governing the dispersion of the sediment seaward of the mouth section.

One of the identified causes of eutrophication of Los Molinos reservoir is the nutrient loading by rivers, especially after wildland fire events (Fernandez et al. 2010). However, the ability to monitor the fate and transport of those polluted river plumes in ways that are useful for their prediction remains inadequate. This paper evaluates the applicability of multitemporal Landsat data for monitoring an enriched, post-fire turbid river plume that enters a medium-sized reservoir by using different techniques through a varying level of available information.

2 Field Data

2.1 In Situ Data

Los Molinos reservoir lies in the semi-arid, central region of Argentina between the latitudes of 31°45′S and 31°55′S and the longitudes 64°25′W and 64°35′W (Fig. 1). It is a relatively

narrow waterbody (3 km wide and 12 km long) whose major axis is aligned parallel to the prevailing wind directions (i.e. North - South).

The reservoir's catchment area is 978 km^2 and can be divided in four sub-basins as illustrated in Fig. 1. The main inflow tributary to the reservoir is Los Espinillos River that contributes with the 45 % of the total water inflow to the reservoir.

High temperatures, drought and strong winds are typical during spring season (from September to December), and frequently those conditions result in fire events within the catchment. In particular, this study is based on the fire that affected Los Molinos' watershed on September, 2003. According to Fig. 2, this fire event was followed by a severe drought which lasted for 6 months. Then, by the middle of November to beginning of December, 80 mm rain falling caused a major flood on the main reservoir's tributary, Los Espinillos river, with a total discharge, Q_t, that reached the 5.56 m^3/seg on December 9, 2003. As a consequence, fine suspended sediment (0.2–60 μm in diameter) mass concentrations, *SSC*, measured along this tributary rose to 100 mg/l, while turbidity, *T*, to 20 NTU, and organic carbon, *OC*, to 11.5 mg/l.

Figure 2 further indicates that both turbidity and phosphorus increased considerably during the first inflow that propagates into the reservoir after the fire-episode. This may leaded to an enhanced nutrient flux into the reservoir affecting habitats and organisms, as in the study cases of Florsheim et al. 1991 and Reneau et al. 2007.

2.2 Satellite Data

Two passive satellite sensors were used in this study to assess the *SSC* values. The Thematic Mapper (TM) that uses the Landsat 5 satellite as platform, and the Enhanced Thematic Mapper

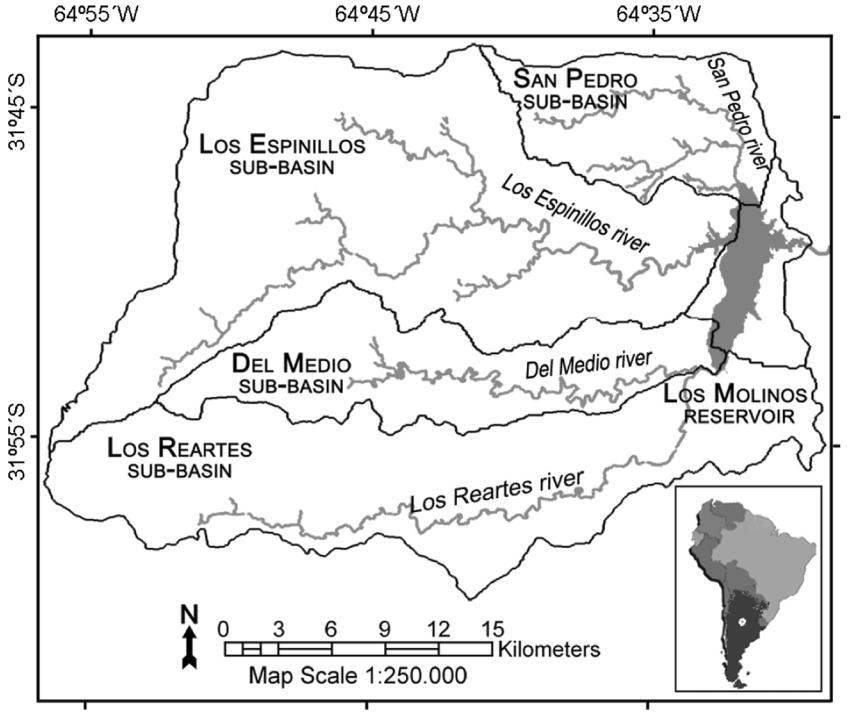

Fig. 1 Location of Los Molinos reservoir and its watershed in Cordoba province, Argentina

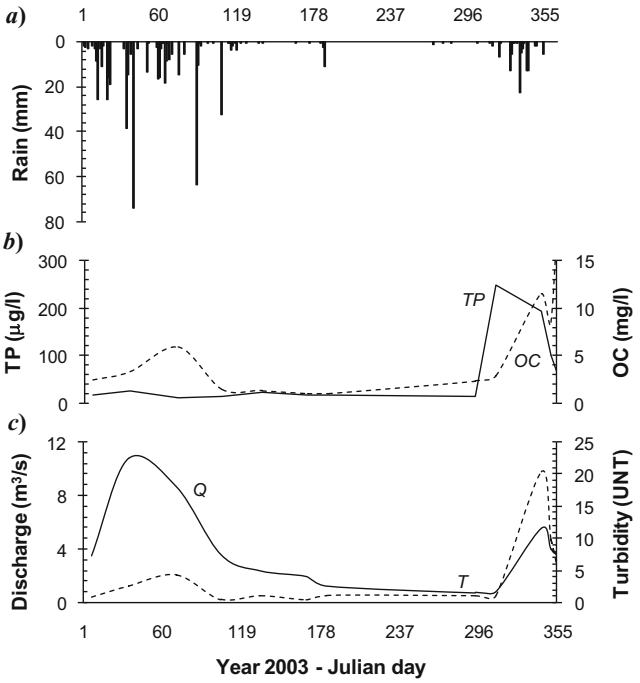

Fig. 2 Los Espinillos river conditions from discrete sampling measurements during year 2003: **a** area weighted rainfall amount in watershed; **b** and **c** measured parameters at the river discharge site

Plus (ETM+) which is onboard Landsat 7 satellite. The analyzed remote-sensing data source consisted of four TM images and five ETM+ images, as listed in Table 1. All image processing steps were carried out using ENVI image processing system (see Herting et al. 2004). Also, a RGB band combination (1,6,6) was used to detect haze and cloud cover. The images with cloud presence over the study area were not used, so that two TM and four ETM+ images were finally used during the SSC mapping. Regarding the identification of burned areas along the watershed, two of the free clouds ETM+ images were analyzed as pre-fire scene: Julian day 295 (October 22, 2003), and post-fire scene: day 343 (December 9, 2003).

Table 1 Acquisition date of path 229 row 82 Landsat time series used in this study

Date	Sensor type	Sky condition
04/13/2003	ETM+	Free-clouds
10/22/2003	ETM+	Free-clouds
11/07/2003	ETM+	Free-clouds
11/15/2003	TM	Presence of clouds
12/01/2003	TM	Presence of clouds
12/09/2003	ETM+	Free-clouds
12/17/2003	TM	Free-clouds
12/25/2003	ETM+	Free-clouds
02/01/2004	TM	Free-clouds

2.2.1 Cross-Calibration of TM Images

Although TM and ETM+ bands are commonly considered to be comparable, previous studies have demonstrated important differences, suggesting the need to apply cross-calibration procedures (Vicente-Serrano et al. 2008). Vogelmann et al. (2001) developed a simple procedure to cross-calibrate the TM images. As proposed by these authors, the empirically derived slope and intercept values for each band were used to convert the TM to ETM+DN, so that $DN_{ETM+}=Slope\times DN_{TM}+Intercept$.

2.2.2 Radiometric Correction

Radiometric correction aims to transform imaging data from multiple sensors and platforms into a common radiometric scale, and to reduce signal variations unrelated to the brightness of the imaged surface (Sriwongsitanon et al. 2011). Once the cross-calibration of TM data was done, at-sensor spectral radiance for band λ, L_λ (in W/m^2/sr/μm), was calculated by considering $L_\lambda=G\times DN+B$, where G is the band-specific rescaling gain factor and B is the band-specific rescaling bias factor (Huang et al. 2002). Both G and B values can be found in the header file of each image.

2.2.3 Atmospheric Correction

The electromagnetic radiation signal collected by satellites is modified by the scattering and absorption processes due to the gases and aerosols present in the atmosphere (Song et al. 2001). Several algorithms have been developed to correct those atmosphere effects (Ouaidrari and Vermote 1999; Gao et al. 2009). This study considered the widely used Dark-Object Subtraction model (DOS) written as

$$\rho = \frac{\pi * \left(L_\lambda - L_\rho\right) * d^2}{T_V * \left(E_0 * \cos(O_Z) * T_Z\right) + E_{down}} \tag{1}$$

Where ρ is the surface reflectance, L_p is the path radiance, d^2 is the Earth-sun distance in astronomical units, T_V is the atmospheric transmittance from the target toward the sensor, E_0 is the exoatmospheric solar constant, θ_z is the solar zenith angle, T_z is the atmospheric transmittance in the illumination direction and E_{down} is the downwelling diffuse irradiance. The values of the above parameters can be found in Chavez (1996), Song et al. (2001) and Huang et al. (2002).

2.2.4 Geometric Correction

Geometric correction aims to remove geometric distortions introduced by a variety of factors which vary for each image acquisition event. This procedure ensures individual picture elements (pixels) are placed in their proper planimetric map location (Sriwongsitanon et al. 2011). Image to image rectification was done, using as base images georeferenced scenes. In the reference process, a number of more than 80 ground control points (GCPs) well distributed were used for each image. The root mean square error (RMSE) for positional accuracy was less than 15 m (0.5 pixel) for all images, guaranteeing a precise geometric match among them. All satellite images were projected into Argentina (POSGAR 94) Zone 3 with the WGS-84 datum.

3 Study Method

3.1 *SSC* Assessment

The multitemporal Landsat dataset listed earlier in Table 1 was analyzed to assess the spatial and temporal patterns of the *SSC* values across the reservoir. Due to the lack of in situ *SSC* samples within the waterbody, and in order to ensure a robust *SSC* distribution, processing techniques such as digital enhancement tools (histogram equalization) were performed to select the combination of bands which gave the best information on the SSC distribution. Hence, the visual enhancement techniques applied on each band combination of multitemporal Landsat series showed that the sum of the three following optical bands: red (band 3: 0.63 to 0.69 μm), near infrared (band 4: 0.76 to 0.90 μm) and short infrared (band 5: 1.55–1.75 μm) had the best spectral response to the *SSC* values, as shown in Fig. 3. This figure clearly shows that as wavelength increases, response values are higher for suspended solids in the water column. Therefore, for band 3 and superior it was possible to differentiate more clearly areas of higher and lower sediment concentrations. Furthermore, the addition of bands 3, 4 and 5 was the best combination to represent the changes in both: the hue of suspended solids, and the greater differentiation around the higher reflectance values.

Previous studies have shown that the combination of Landsat bands 3 and 4 can provide useful information when large sediment loads occur in aquatic systems (Giardino et al. 2001). Results presented here indicated that by adding band 5 to the mentioned model the grades were strengthened. This observation was then validated by analysing a selected transects on the

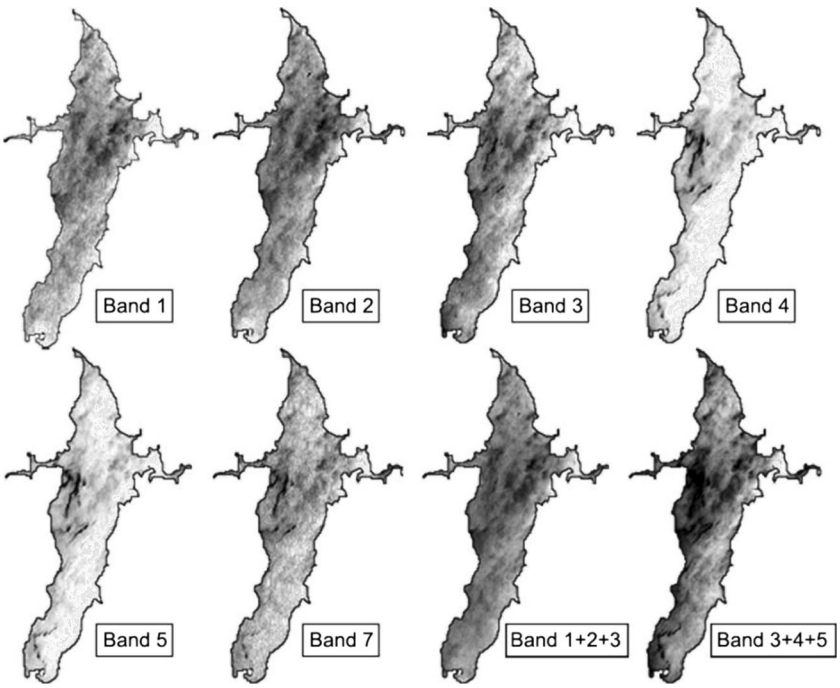

Fig. 3 Different combinations of bands that were examined for the December 9, 2003 ETM+ image to represent the *SSC* values on Los Molinos reservoir. As clearer water has less reflectance than turbid water, higher reflectivity areas represented higher values of *SSC*

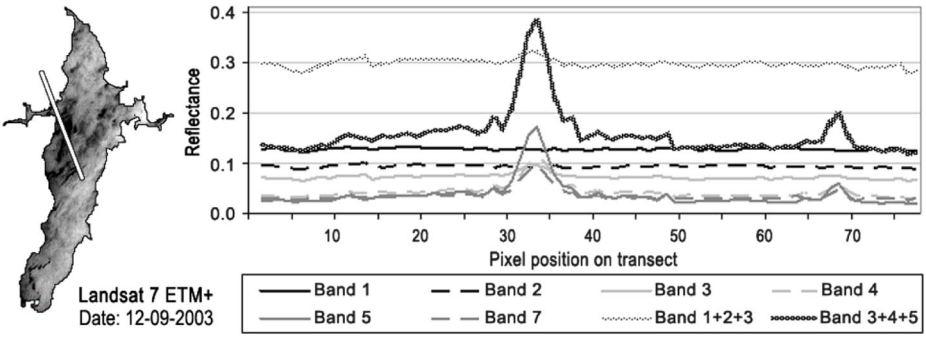

Fig. 4 Reflectance profiles for different bands and combinations tested on the December 9, 2003 ETM+ image. Figure on the left represents the generated transect which includes the area where the higher reflectance values were observed

region of higher reflectance. Hence, Fig. 4 clearly identifies the highest increase in the reflectance values within the areas in which the higher value of *SSC* would be expected for the combination of bands 3,4,5. This result was observed then in all the images analyzed in this study, suggesting the presence of a zone with high solids accumulation (in which a large number of particles in suspension were located) and confirming that such a combination of bands was the best assessment technique of the turbid surface plume in the reservoir.

By using the proposed theoretical model, the *SSC* values were determined in Fig. 5. Complementary, Fig. 6 show the pixel distributions corresponding to the *SSC* maps for each

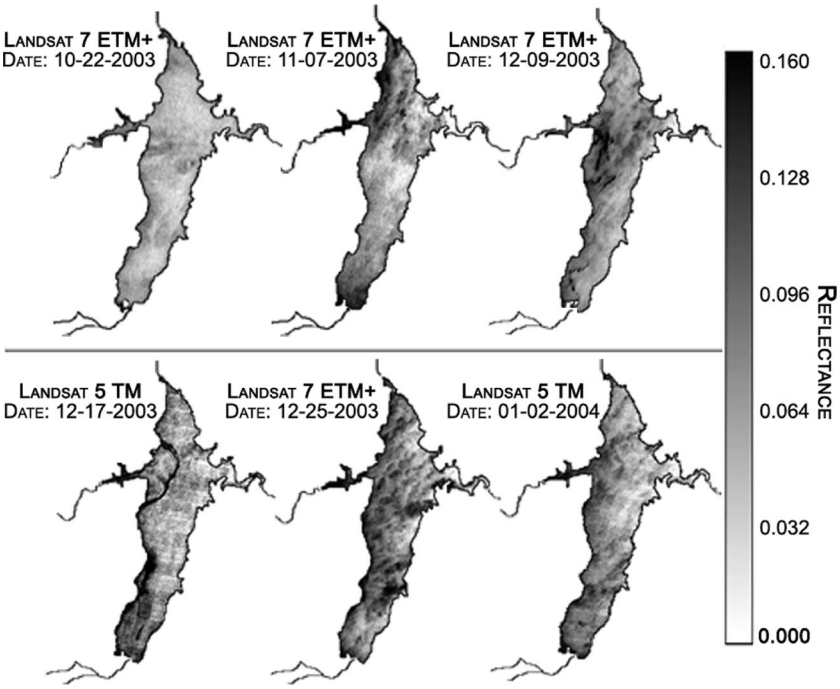

Fig. 5 *SSC* maps of Los Molinos reservoir derived from multitemporal remote sensing satellite images

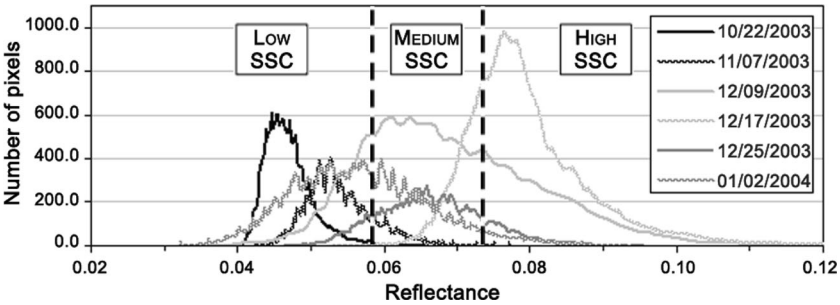

Fig. 6 Radiometric distribution for the selected Landsat images. The vertical lines represent the threshold of each *SSC* category

satellite image. Based on this reflectance distribution, the threshold classes generated with the applied model resulted in the qualitative quantification of the *SSC* values of Fig. 7.

3.2 Scaling Analysis

Based on the in-situ mouth river conditions, the location of the plunging point and the effects of both the wind and time-varying discharge on the spreading of the surface plume were analyzed by using a set of simplified existent empirical expressions. This analysis considered the period in between Julian days 311 (November 7, 2003) and 359 (December 9, 2003) and results were contrasted with the spatial and temporal plume patterns observed on the satellite images available for the study period.

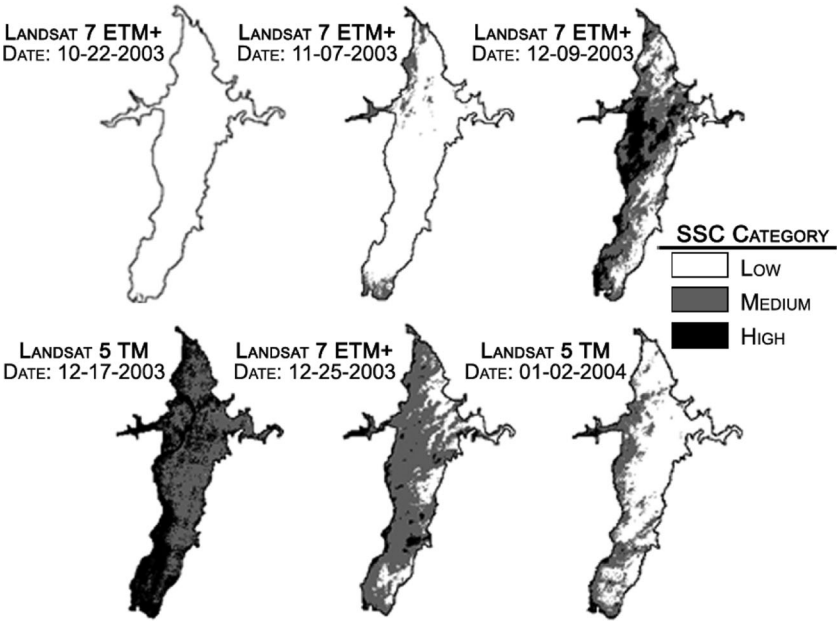

Fig. 7 Qualitative *SSC* scale maps derived from the multitemporal Landsat images

3.2.1 Criteria for Plunging

When except for the concentration of suspended sediment, the river water is assumed to have the same density as the sediment-free reservoir water, it is possible to assess the densimetric Froude number $F_D=U/(RgCh)^{0.5}$, in which U denotes the riverine plume mean velocity, R is the submerged specific gravity of the sediment (~1.6 for quartz), g is gravitational acceleration, C is defined as $C=Q_s/(Q_w+Q_s)$, so denoting the volume concentration of suspended sediment flowing into the reservoir, and h is the mean thickness of the flow. Q_w and Q_s denote the water and sediment inflow rate, respectively.

The position of the plunge point was estimated then by equating F_D and the Froude number at the location of the plunge point, F_P (Imberger and Patterson 1990; Chung et al. 2009). Regarding F_P, for a triangular cross-section with a half-angle (θ), Hebbert et al. (1979) proposed

$$F_P \approx \frac{\sin(\theta)\tan(S_o)}{0.25(f_i+f_b)}\left(1-0.85\times\frac{\sqrt{f_i+f_b}}{2}\sin(\theta)\right) \tag{2}$$

Based on Ford and Johnson (1983) f_b and f_i values were assumed to be 0.02 and 0.004, respectively, while the bottom slope $S_o=0.0004$ and $\theta=87°$ were estimated from the reservoir bathymetry data. The hydraulic depth (h_p) at the plunge point was then estimated as

$$h_p = \left[\frac{2Q_t^2}{F_P^2 RCg\tan^2(\theta)}\right]^{1/5} \tag{3}$$

Where $Q_t=Q_w+Q_s$, so denoting the total inflow rate (in m^3/s).

3.2.2 Wind and River Discharge Influence

The wind-driven velocity at the reservoir surface was scaled for hourly average wind speeds within the period of 12 h previous to time of satellite images using equation $U_{wind}=[(\rho_a/\rho)C_{10}]^{0.5}U_{10}$, where ρ_a is the atmospheric density, ρ the density of the water at the reservoir surface, C_{10} the surface drag coefficient (~1.3×10^{-3}), and U_{10} the wind speed at 10 m above the water surface. The satellite images were obtained at approximately 8:45 a.m. The low to strong wind speed ranged from 0.5 to 15 m/s, with mean values of 0.5 to 3 m/s, as indicated below in Table 2. The analysis included the mean directions (coming from the North, Northeast and East). To scale the relative strengths of the wind and river discharges forcing on the plume dynamics, the ratio in between the wind-driven and buoyancy-driven velocity scales U_{wind}/u_{dis} was estimated based on Whitney and Garvine (2005). The buoyancy-driven velocity scale was approximated by

$$u_{dis} = \frac{1}{K}(2gRCQ_t f)^{1/4} \tag{4}$$

Where f denotes the Coriolis frequency (set at 0.9×10^{-4} 1/s) and K indicates the Kelvin number, $K=L_w/R_b$, where L_w is the river width and R_b is the baroclinic Rossby radius, $R_b=(gRC)^{0.5}/f$ (Garvine 1995). Hence, wind forcing should dominate when the ratio U_{wind}/u_{dis} is larger than 1.

Table 2 Geometric parameters and length scales used to typify imagery data

	Julian day			
Key parameters	311	343	351	359
Specific parameters (river mouth)				
Q_t (m^3/s)	0.87	5.56	4.11	3.10
SS (mg/l)	0.86	99.11	33.07	7.19
Excess (kg/m^3)	$5.4\ 10^{-4}$	$6.2\ 10^{-2}$	$2.1\ 10^{-2}$	$1.7\ 10^{-3}$
RCg (m/s^2)	$5.3\ 10^{-6}$	$6.4\ 10^{-4}$	$2.1\ 10^{-4}$	$1.7\ 10^{-5}$
U (m/s)	0.02	0.09	0.07	0.05
F_D	7.6	4.4	5.7	15.1
Derived parameters				
h_p	14.6	9.5	12.3	21.7
U_{10}	6	5	0.5	3
U_{wind}	0.16	0.13	0.01	0.08
R	88	971	552	157
K	1.13	0.10	0.18	0.63
M (m^4/s^2)	0.87	5.56	4.11	3.10
J	0.86	99.11	33.07	7.19
LM	29.49	17.18	22.28	59.22
Lm	1.32	10.15	74.85	28.30
u_{dis}	0.002	0.137	0.055	0.008
U_{wind}/u_{dis}	66.87	0.96	0.24	10.30

3.2.3 Sediment Resuspension

To examine the correlation between wind speed and sediment resuspension, the hourly-mean surface winds at this reservoir was considered for the previous 12 h to the time of the satellite images. Based on the wind data, the effective fetch was computed by the modified method of Saville (1954). The relationship between wind speed and wave height was assessed then by using the empirical formulation (CERC 1984)

$$\frac{hH}{U_{10}^2} = 0.283\tanh\left[0.53\left(\frac{gd}{U_{10}^2}\right)^{3/4}\right]\tanh\left[\frac{0.00565\left(\frac{gF}{U_{10}^2}\right)^{1/2}}{\tanh\left[0.53\left(\frac{gd}{U_{10}^2}\right)^{3/8}\right]}\right] \tag{5}$$

While the wave period T and wave length L were estimated using the equations (CERC 1984)

$$\frac{gT}{U_{10}} = 7.54\tanh\left[0.833\left(\frac{gd}{U_{10}^2}\right)^{3/8}\right]\tanh\left[\frac{0.0379\left(\frac{gF}{U_{10}^2}\right)^{1/2}}{\tanh\left[0.833\left(\frac{gd}{U_{10}^2}\right)^{3/8}\right]}\right] \tag{6}$$

$$L = \frac{gT^2}{2\pi}\tanh\frac{2\pi d}{L} \tag{7}$$

In which F is the fetch length of wind (m). Hence, the bed shear stress exerted by wind-induced wave τ_w was calculated by

$$\tau_w = H\left[\rho\frac{\left(\nu\left(\frac{2\pi}{T}\right)^3\right)^{0.5}}{2\sinh\left(\frac{2\pi d}{L}\right)}\right] \tag{8}$$

Although sediment resuspension in wind-exposed reservoirs is caused by the bed stress associated with the combination of near-bed wave orbital velocity, near-bed current velocity and internal seiches, in shallow waterbodies the most important forcing to induce resuspension is the bed shear stress generated by surface waves (Luettich et al. 1990; Hawley and Lesht 1992; Mian and Yanful 2004). Hence, results from Eq (8) were used here to assess sediment resuspension areas within the reservoir, disregarding the influence of the other mentioned processes.

4 Results and Interpretations

4.1 The *SSC* Spatial and Temporal Variability

Before the rains that took place on November (Fig. 2) the reservoir had a low and homogeneous distribution of *SSC* (see Fig. 7). On November 7, 2003 and after the falling rain, it was observed the beginning of a high reflectance influx through Los Espinillos river. Less intensity inputs were observed for the San Pedro river on the North, and for the confluence of the Del Medio and Los Reartes rivers on the Southern reservoir area. The increase in water reflectivity observed on the images was due to the presence of flows with high concentrations of suspended sediments produced by the fire in the previous weeks to the flood event.

On December 9, 2003, the areas with higher *SSC* category were larger, as it is suggested by the *SSC* spatial distribution of Fig. 7 and by the bar graph of Fig. 8. For this particular day, 49.2 % and 23.45 % of the reservoir surface was classified with a medium and a high SSC category, respectively. Regarding December 17, 2003, the maximum value of *SSC* was observed along the Southwest coastal area. The 47.8 % of the surface was classified with a high *SSC* category, while the 51.7 % was classified with a medium *SSC* category. On December 25, 2003, a medium *SSC* category was observed over the entire surface of the reservoir. By January 2, 2004, the reflectance values decreased due to the sedimentation of

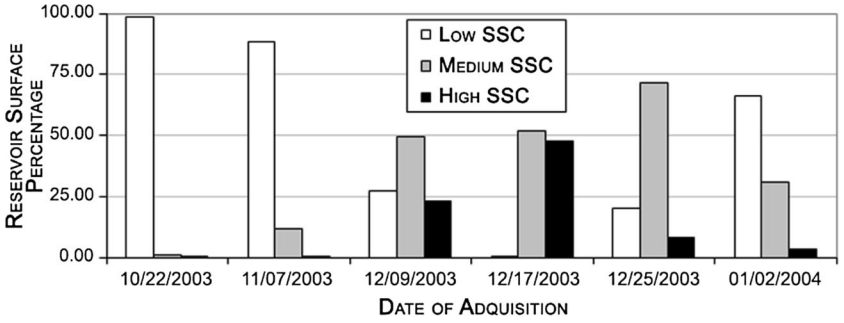

Fig. 8 Percentage of reservoir surface with different SSC categories

suspended matter, and therefore the low *SSC* category dominated in the reservoir, as illustrated in Figs. 7 and 8.

Alternatively, Fig. 9 shows the spatial distribution of the surface values of *SSC* for four selected images; the maximum reflectance value to be equivalent to the maximum value of 100 % of *SSC*. For the selected 4 days, Table 2 lists then the specific and derived plume parameters that were assessed based on the wind conditions and river mouth characteristics (width: 500 m, averaged depth: 9 m). During flood, river and reservoir water conditions were isothermals, whereas the inflow turbidity increased up to 99 NTU (Fig. 2).

To locate where the inflow current plunged due to density differences, the densimetric Froude number $F_D=U/(RgCh)^{0.5}$ was estimated (Table 2) based on the available in-situ data. On days November 7 and December 25, F_D reached the values 7.6 and 15.1, respectively, indicating a large inertial force compared to the buoyancy force, and with the submersion point occurring well into the reservoir. Further, Eq (3) predicted the location of the plunge point in a section with a depth of h_p=14.6–21.7 m, i.e. between 1 and 2.5 km respectively downstream of the inflow boundary (according to the bathymetry data). Significantly, the characterization of the plume behavior computed in Table 2 validated well the plume dynamics suggested by the *SSC* distributions of the satellite images of Fig. 9.

Complementary, the larger values observed for both Q_t and *SSC* on December 9, resulted in a value of h_p~4.4, similar to the one on day December 17, h_p~5.7 (Table 2). However, that is not observed in the image of Fig. 9b probably due to surface turbidity caused by the wind-driven turbulence, as it is analyzed below.

4.2 The Combined Effect of Discharge and Wind Stress

The ratio of the wind influence to river discharge forcing assessed according to Eq (4) is also listed in Table 2. River discharge forcing dominates when the magnitude of the ratio U_{wind}/u_{dis} is less than 1. This is suggested by Fig. 9c on December 17, 2003, when the plume became radially dispersed at about 1 km from the river mouth. When the ratio U_{wind}/u_{dis} exceeds 1, the wind contribution is stronger than buoyancy influence and the turbid river plume becomes wind-driven, as it is shown clearly on November 7 (Fig. 9a) and on December 25 (Fig. 9d). Based on the previous results, wind-driven currents played an important role in the development and transport of the observed surface plume.

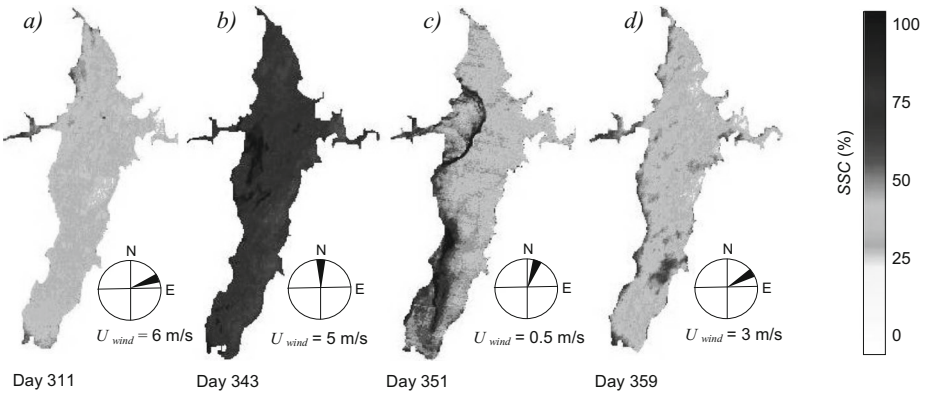

Fig. 9 Suspended sediment fields during the flood event from Landsat imagery data: **a** early in the event, **b** during high river discharge and peak winds, **c** during relatively high river discharge rate and low winds, and **d** during low discharge, near the end of the event

Complementary, the dominant regimes of the turbid plume were assessed by considering that they were largely dictated by the river mouth conditions: the total river discharge Q_t, the momentum $M=Q_tU$ and the buoyancy $J=Q_tgRC$ (e.g. Jirka et al. 1981, Jones et al. 2007). The magnitude of the two derived scales listed then in Table 2: $L_M=M^{3/4}/J^{1/2}$, which measures the region in which jet-like mixing dominates to where buoyancy induced lateral spreading prevails, and $L_m=M^{1/2}/J^{1/2}$, which designates the point where the flow becomes strongly influenced by the ambient surface currents, they leaded to insight on the dynamics of the river plume into the reservoir that agreed well with its behavior assessed earlier in this section. Based on this proposed length scale analysis, the inflow observed in Fig. 9 may be characterized as a buoyant dominated surface discharge which evolved from a buoyant-jet current dominated on day November 7 to a free buoyant-jet on December 17.

4.3 The Effect of Wind Induced Wave on Sediment Resuspension

In the absence of available field data, estimates for the wind wave conditions across the reservoir were made by applying the Saville method (1984). Based on the results, winds that originated from the East on December 25, 2003, gave the higher wave heights along the west coastline of the reservoir. Due to the relative long wind fetch (Fig. 10a) and shallow depth (~3–5 m), the wave induced bottom shear stress computed by Eq (8) was greater t within this coastline area, as illustrated by Fig. 10b. Then, by comparing Fig. 10b with the sediment surface concentration of Fig. 9d, it is shown that sediment resuspension at the time of the

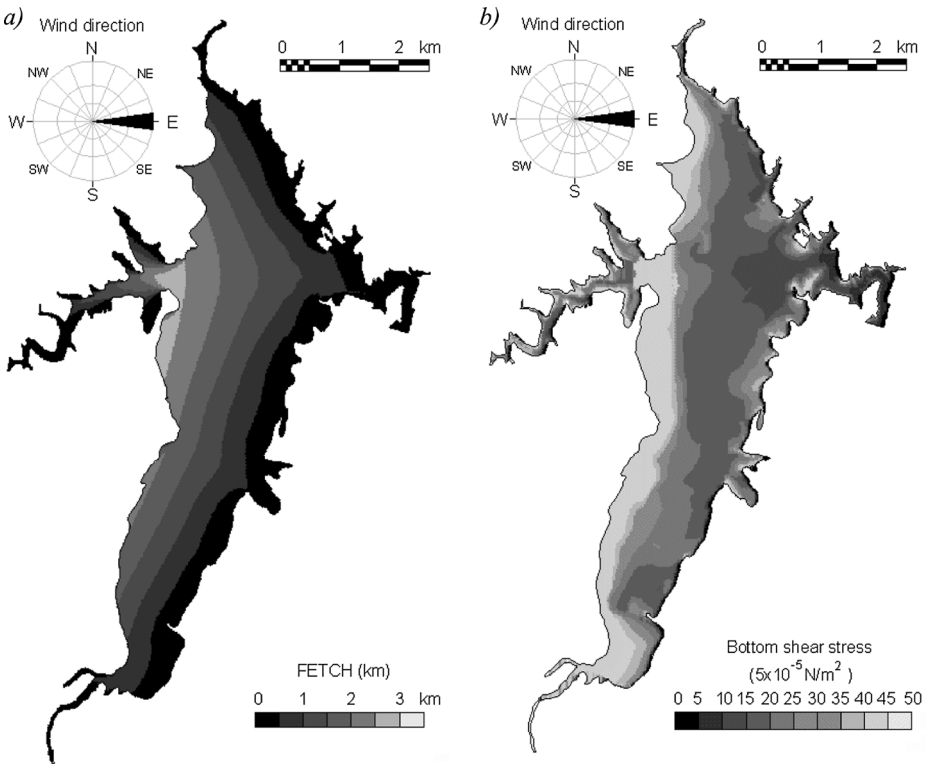

Fig. 10 Computed (**a**) fetch, and (**b**) bottom shear stress for Los Molinos reservoir on December 25, 2003

satellite image mainly occurred in the southern part and along the east shore of the lake, which is consistent with the higher bottom shear stress values observed in Fig. 10b. These results suggested that wave action was the dominant factor in sediment resuspension in the reservoir on December 25, 2003.

5 Conclusions

The dynamics of a turbid plume into Los Molinos reservoir under varying ambient conditions during a flood event was investigated by using a combination of both in-situ river data together with satellite imagery data.

By combining bands 3, 4 and 5 it was possible to discriminate the most slightly changes of reflectance on the surface of the reservoir. The dispersal mechanisms of the observed turbid plume were then assessed by computing a set of parameters based on river mouth conditions that agreed well with those observed on the satellite images.

Particularly, results illustrated here that suspended solids during flooding events are regulated by river mouth conditions, and empirical models can predict the resulting plume behavior. This may provide managers with the capacity to decide when to implement water diversion during post-fire storm events based on river mouth data. Further, the methodology proposed here can be adopted as an assisting tool to reach systems where minor field-measured information on suspended sediment concentration is available.

References

Alcantara E, Stech J, Lorenzzetti J, Bonnet M, Casamitjana X, Assireu A, Novo E (2010) Remote sensing of water surface temperature and heat flux over a tropical hydroelectric reservoir. Remote Sens Environ 114(11):2651–2665

CERC (1984) Coastal Engineering Research Center. Shore protection manual. Waterways Experiment Station, US Army Corps of Engineers

Chavez P (1996) Image-based atmospheric corrections revisited and improved. Photogramm Eng Remote Sens 62:1025–1036

Choubey V (1994) Monitoring water quality in reservoirs with IRS-1A-LISS-I. Water Resour Manag 8(2):121–136

Chung E, Hipsey M, Imberger J (2009) Modelling the propagation of turbid density inflows into a stratified lake: daecheong reservoir, Korea. J Environ Model Softw 24:1467–1482

Cohen W, Goward S (2004) Landsat's role in ecological applications of remote sensing. Bioscience 54(6):535–545

Fernandez R, Lasso R, Furbatto C, Larrosa N (2010) "Modelación por la contaminación por fuentes difusas en la cuenca hídrica del embalse Los molinos" XXIV latinoamerican congress. Punta del Este, Uruguay

Florsheim J, Keller E, Best D (1991) Fluvial sediment transport in response to moderate storm flows following chaparral wildfire, southern California. Geol Soc Am Bull 103:504–511

Ford D, Johnson M (1983) An assessment of reservoir density currents and inflow processes. Technical report E-83-7, U.S. Army Corps of Engineering Waterways Experiment Station, Vicksburg

Gao B, Montes M, Davis C, Goetz A (2009) Atmospheric correction algorithms for hyperspectral remote sensing data of land and ocean. Remote Sens Environ 113(1):517–524

Garvine R (1995) A dynamical system for classifying buoyant coastal discharges. Cont Shelf Res 20:2067–2093

Giardino C (2010) Application of remote sensing in water resource management : the case study of lake Trasimeno, Italy. Water Resour Manag 24(14):3885–3899

Giardino C, Pepe M, Brivio P, Ghezzi P, Zilioli E (2001) Detecting chlorophyll, secchi disk depth and surface temperature in a sub-alpine lake using landsat imagery. Sci Total Environ 268(1–3):19–29

Han Z, Jin Y, Yun C (2006) Suspended sediment concentrations in the Yangtze River estuary retrieved from the CMODIS data. Int J Remote Sens 27(19):4329–4336

Hawley N, Lesht BM (1992) Sediment resuspension in Lake St Clair. Limnol Oceanogr 37(8):1720–1737. doi: 10.4319/lo.1992.37.8.1720

Hebbert B, Imberger J, Loh I, Petterson J (1979) Collie River underflow into the Wellington Reservoir. J Hydraul Div ASCE 105:533–545

Hellweger F, Miller W, Oshodi K (2006) Mapping turbidity in the Charles River, Boston using a high resolution satellite. Environ Monit Assess 132(1–3):311–320

Herting A, Farmer T, Evans J (2004) Mapping of the evaporative loss from elephant butte reservoir using remote sensing and GIS technology. Technical report. States University (NMSU, CAGE), New Mexico

Hu C, Muller-Karger F, Andrefouet S, Carder K (2001) Atmospheric correction and cross-calibration of LANDSAT-7/ETM+ imagery over aquatic environments: a multiplatform approach using sea WiFS/MODIS. Remote Sens Environ 78(1–2):99–107

Huang C, Zhang Z, Yang L, Luylie B, Homer C (2002) MRLC 2000. Image Preprocessing Procedure, USGS

Imberger J, Patterson JC (1990) Physical lumnology. Adv Appl Mech 27:303–475

Jirka GH, Adams EE, Stolzenbach KD (1981) Buoyant surface jets. J Hydr Div 10711:1467–1487

Jones G, Nash D, Doneker L, Jirka H (2007) Buoyant surface discharge into water bodies. I: flow classification and prediction methodology. J Hydraul Eng 133:1010–1020

Kloiber S, Brezonik P, Olmanson L, Bauer M (2002) A procedure for regional lake water clarity assessment using Landsat multispectral data. Remote Sens Environ 82(1):38–47

Luettich RA Jr et al (1990) Dynamic behavior of suspended sediment concentrations in a hallow lake perturbed by episodic wind events. Limnol Oceanogr 35(5):1050–1067. doi:10.4319/lo.1990.35.5.1050

Mian M, Yanful E (2004) Analysis of wind-driven resuspension of metal mine sludge in a tailings pond. J Environ Eng Sci 3:119–135

Miller J, Yool S (2002) Mapping forest post-fire canopy consumption in several overstory types using multi-temporal Landsat TM and ETM data. Remote Sens Environ 82(2–3):481–496

Ostlund C, Flink P, Strombeck N, Pierson D, Lindell T (2001) Mapping of the water quality of lake Erken, Sweden, from imaging spectrometry and Landsat thematic mapper. Sci Total Environ 268(1–3):139–154

Ouaidrari H, Vermote E (1999) Operational atmospheric correction of Landsat data. Remote Sens Environ 70(1):4–15

Parker G, Toniolo H (2007) Note on the analysis of plunging of density flows. J Hydraul Eng 133(6):690–694

Pavelsky T, Smith L (2009) Remote sensing of suspended sediment concentration, flow velocity, and lake recharge in the Peace-Athabasca Delta, Canada. Water Resour Res 45:W11417. doi:10.1029/2008WR007424

Peckham S (2008) A new method for estimating suspended sediment concentrations and deposition rates from satellite imagery based on the physics of plumes. Compt Rendus Geosci 34(10):1198–1222

Reneau SL, Katzman D, Kuyumjian GA, Lavine A, Malmon DV (2007) Sediment delivery after a wildfire. Geol Soc Am 35(2):151–154

Saville T (1954) The effect of Fetch width on wave generation. *Journal Technical Memorandum*, 70

Schmugge T, Kustas W, Ritchie J, Jackson T, Rango A (2002) Remote sensing in hydrology. Adv Water Resour 25(8–12):1367–1385

Shukla J, Misra A, Chandra P (2008) Modeling and analysis of the algal bloom in a lake caused by discharge of nutrients. Appl Math Comput 196(2):782–790

Smith V, Tilman G, Nekola J (1999) Eutrophication: impacts of excess nutrient inputs on freshwater, marine, and terrestrial ecosystems. Environ Pollut 100(1–3):176–196, Oxford, U. K

Song C, Woodcock C, Seto K, Lenney M, Macomber S (2001) Classification and change detection using Landsat TM data: when and how to correct atmospheric effects? Remote Sens Environ 75(2):230–244

Sriwongsitanon N, Surakit K, Thianpopirug S (2011) Influence of atmospheric correction and number of sampling points on the accuracy of water clarity assessment using remote sensing application. J Hydrol 401(3–4):203–220

Vicente-Serrano S, Pérez-Cabello F, Lasanta T (2008) Assessment of radiometric correction techniques in analyzing vegetation variability and change using time series of Landsat images. Remote Sens Environ 112(10):3916–3934

Vogelmann J, Helder D, Morfitt R, Choate M, Merchant J, Bulley H (2001) Effects of landsat 5 thematic mapper and landsat 7 enhanced thematic mapper plus radiometric and geometric calibrations and corrections on landscape characterization. Remote Sens Environ 78(1–2):55–70

Whitney M, Garvine R (2005) Wind influence on a coastal buoyant outflow. J Geophys Res 110:C3014. doi:10.1029/22003JC002261

Wu G, de Leeuw J, Liu Y (2009) Understanding seasonal water clarity dynamics of Lake Dahuchi from in-situ and remote sensing data. Water Resour Manag 23(9):1849–1861